UCLA
UCLA Previously Published Works

Title

pH-dependent gating mechanism of the *Helicobacter pylori* urea channel revealed by cryo-EM.

Permalink

https://escholarship.org/uc/item/47c16967

Journal

Science advances, 5(3)

ISSN

2375-2548

Authors

Cui, Yanxiang
Zhou, Kang
Strugatsky, David
et al.

Publication Date

2019-03-01

DOI

10.1126/sciadv.aav8423

Peer reviewed

eScholarship.org Powered by the California Digital Library
University of California

BIOCHEMISTRY

pH-dependent gating mechanism of the *Helicobacter pylori* urea channel revealed by cryo-EM

Yanxiang Cui[1,2]*, Kang Zhou[1,2]*, David Strugatsky[3], Yi Wen[4], George Sachs[4], Z. Hong Zhou[1,2]†, Keith Munson[4]

Copyright © 2019 The Authors, some rights reserved; exclusive licensee American Association for the Advancement of Science. No claim to original U.S. Government Works. Distributed under a Creative Commons Attribution NonCommercial License 4.0 (CC BY-NC).

The urea channel of *Helicobacter pylori* (*Hp*UreI) is an ideal drug target for preventing gastric cancer but incomplete understanding of its gating mechanism has hampered development of inhibitors for the eradication of *H. pylori*. Here, we present the cryo-EM structures of *Hp*UreI in closed and open conformations, both at a resolution of 2.7 Å. Our hexameric structures of this small membrane protein (~21 kDa/protomer) resolve its periplasmic loops and carboxyl terminus that close and open the channel, and define a gating mechanism that is pH dependent and requires cooperativity between protomers in the hexamer. Gating is further associated with well-resolved changes in the channel-lining residues that modify the shape and length of the urea pore. Site-specific mutations in the periplasmic domain and urea pore identified key residues important for channel function. Drugs blocking the urea pore based on our structures should lead to a new strategy for *H. pylori* eradication.

INTRODUCTION

The gastric pathogen *Helicobacter pylori* afflicts most of the global population (*1*) and increases the risk of gastric carcinoma, the third-leading cause of cancer deaths worldwide (*2*–*9*). In 2014, the World Health Organization recommended *H. pylori* eradication as a strategy for preventing gastric cancer (*10*). However, current *H. pylori* eradication methods require the use of multiple antibiotics that has resulted in decreasing efficacy as antibiotic resistance rises. An alternative strategy for eradication would be the use of a single drug to inhibit urea entry and eliminate bacterial survival in the gastric environment. Urea transit through *H. pylori*'s urea channel, *Hp*UreI, is controlled by pH-dependent gating, i.e., channel closure at neutral pH and opening in response to external acid to allow urea entry into the cytoplasm. Urea hydrolysis by cytoplasmic urease then generates ammonia and carbonic acid that ultimately buffer the periplasmic space to pH 6.1, enabling the survival of *H. pylori* in the gastric acid (*11*–*14*). Previously reported x-ray crystallography of a 6his-tagged *Hp*UreI (6his*Hp*UreI) yielded a low-pH structure at a resolution of 3.3 Å (*15*) but did not define residues in the periplasmic loops (PLs) critical to pH-dependent gating and failed to reveal the closed conformation. The crystal structure at pH 4.8 is a hexamer in which each of the six protomers of ~21 kDa forms a channel composed of three structurally homologous pairs of transmembrane helices (*15*). The N and C termini are on the periplasmic side of the membrane, thus giving three cytoplasmic loops (CL1, CL2, and CL3) and two periplasmic loops [PL1 (containing the inserted 6-histag) and PL2]. Sequence alignments with *Hp*UreI identified conserved aromatic and aliphatic residues that define a family of putative amide channel proteins, the AmiS channels (*12*, *16*, *17*). One example of this family, *Ss*UreI, is expressed in the oral bacterium *Streptococcus salivarius* and is 64% homologous to *Hp*UreI but contains 14 fewer residues in PL1 and 9 fewer residues in PL2. *Ss*UreI facilitates urea transit equally at both neutral and acidic pH, suggesting that the expanded loops in *Hp*UreI control pH-dependent gating (*18*). In the 6his*Hp*UreI crystal structure (*15*), however, PL1 was not visible and PL2 was poorly resolved. These deficiencies, and the absence of the closed conformation, have prevented the definition of the pH-dependent gating mechanism.

Here, we present the structures of the closed and open conformations both at a resolution of 2.7 Å, determined by cryo–electron microscopy (cryo-EM). Together with the results of [^{14}C]urea influx activities determined for a variety of mutants in xenopus oocytes, these structures establish a detailed gating mechanism for *Hp*UreI that explains pH sensitivity and shows cooperativity between protomers. These results support a new approach for drug development to eradicate *H. pylori*.

RESULTS AND DISCUSSION

Cryo-EM structures of closed and open conformations

A soluble form of 6his*Hp*UreI had to be generated and optimized to achieve high-resolution cryo-EM. The final purification step used gel filtration at pH 7.0 and 4.8 to yield the closed and open conformations, respectively (see Materials and Methods). In both conformations, our cryo-EM data yielded oligomers of six channel protomers arranged in a hexamer with a lipid core at the centers. Imposition of sixfold symmetry then gave the final three-dimensional (3D) reconstructions and extended the resolution of the closed and open channels to 2.7 Å (Fig. 1, figs. S1 and S2, and table S1). To our knowledge, with a monomer size of 21 kDa and a total mass of ~130 kDa, this is the smallest membrane protein resolved to near-atomic resolution by cryo-EM (*19*, *20*). This is notable considering that the channel lacks extramembrane domains, in contrast to other high-resolution cryo-EM structures of membrane proteins that all resorted to extramembrane domains/subunits to help drive image alignment [e.g., (*21*–*25*)]. The density maps reveal well-defined side chains (fig. S3) of the hexamer fully embedded in the amphipol belt (Fig. 1, A to F, and movies S1 and S3) and show clear differences for the two conformations (Fig. 1, C and F).

[1]California NanoSystems Institute, University California Los Angeles, Los Angeles, CA 90095, USA. [2]Department of Microbiology, Immunology, & Molecular Genetics, University of California Los Angeles, Los Angeles, CA 90095, USA. [3]Department of Chemistry and Biochemistry, University of California Los Angeles, Los Angeles, CA 90095, USA. [4]David Geffen School of Medicine, University of California Los Angeles and Greater West Los Angeles Health Care System, Los Angeles, CA 90095, USA.
*These authors contributed equally to this work.
†Corresponding author. Email: hong.zhou@ucla.edu

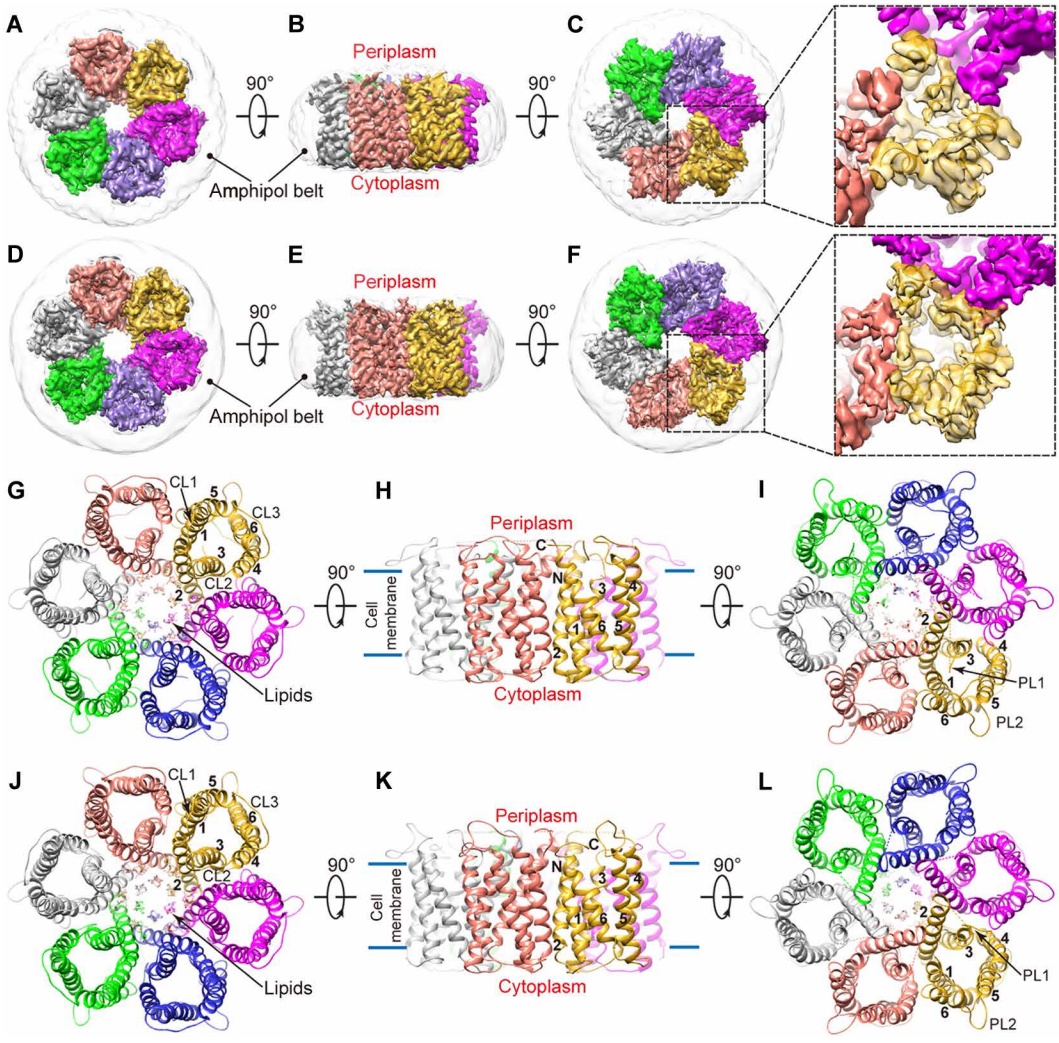

Fig. 1. Cryo-EM density maps and atomic models of 6his*Hp*UreI. (**A** to **F**) Shaded surface views of the cryo-EM density maps of 6his*Hp*UreI in the closed (A to C) and open (D to F) conformations viewed from the cytoplasm (A and D), plane of the membrane (B and E), and periplasm (C and F). Protomers are colored separately, and amphipol is in gray. (**G** to **L**) Ribbon diagrams of the atomic models of 6his*Hp*UreI in the closed (G to I) and open (J to L) conformations viewed as in (A) to (F). Transmembrane helices (TM1 to TM6) are numbered 1 to 6; N and C termini are indicated by N and C; cytoplasmic loops (CL) and periplasmic loops (PL) are labeled CL1 to CL3 and PL1 and PL2, respectively. Lipids are shown as sticks.

Unambiguous atomic models for the closed (Fig. 1, G to I, and movie S2) and open (Fig. 1, J to L, and movie S4) conformations of 6his*Hp*UreI were built and refined on the basis of the high-resolution cryo-EM density maps. Each channel is roughly divided into three sections: a periplasmic domain and vestibule formed by the N and C termini, PL1 and PL2, and the transmembrane helices on the periplasmic side of the urea filter (Fig. 1, I and L); the urea filter near the center of the membrane composed of a ring of side chains from several hydrophobic residues; and a cytoplasmic domain and vestibule composed of the transmembrane helices and loops on the cytoplasmic side of the filter (Fig. 1, G and J).

Comparison of our cryo-EM structures for hexameric 6his*Hp*UreI in the closed and open conformations reveals large-scale differences in the periplasmic domain of the individual protomers, where urea enters the channel and gating is controlled (Fig. 1, C and F). In contrast, only subtle changes occur in the cytoplasmic domain (Fig. 1, G and F). Expanded surface views from the periplasm show increased channel access for the open conformation (Fig. 1, C and F), which are detailed below. Our cryo-EM structures each contain an important segment of PL1 that was totally missing in the crystal structure, and the gating mechanism is revealed by conformational changes in PL1 as well as in PL2 and C terminus, both of which also differ from the crystal.

His^{131} is the pH sensor

The urea transit activity through 6his*Hp*UreI is highest at pH 4.0 and totally lost at pH 7.5, with the midpoint at about pH 6.0 (fig. S8A), which indicates that a histidine residue or residues (with an acid dissociation constant *pKa* of ~6) act as the pH sensor. To sense external acid, these would be expected to be on the periplasmic side and to undergo substantial positional change between the closed or open conformations.

Superimposing the closed and open cryo-EM structures for a single protomer reveals the moving segments of the protein backbone in PL1, PL2, and the C terminus (Fig. 2A and fig. S4). Among

the six histidines exposed on the periplasmic surface, His^{54} and His^{123} show little change between two conformations (Fig. 2, B to E), indicating that neither of these two histidines likely act as a trigger. However, an essential structural role for His^{123}, rather than His^{54}, is suggested by close interaction of His^{123} with the aromatic ring of Tyr^{124}, perhaps stabilizing the proper termination of transmembrane helix 4 (TM4) (Fig. 2, D and E). In contrast, His^{54} lacks side-chain contacts in both closed and open conformations (Fig. 2, B and C). The structural importance of His^{123} is supported by the loss of activity in all of its mutants, whereas both glycine and arginine mutants of His^{54} retain full activity (*26*).

The four histidines located in the moving parts of the structures are His^{70} and His^{71} in PL1, His^{131} in PL2, and His^{193} near the C terminus (Fig. 2, B and C). At the PL1 loop, the double mutant His^{70}Gln-His^{71}Gln showed 60% inhibition at pH 5.0 (fig. S8B) but normal pH-dependent gating. Therefore, His^{70} and His^{71} should have little role in triggering, and the double glutamine substitution only partially compensates for their function in support of urea influx activity. Consistent with this, little interaction involving His^{70} and His^{71} was observed in the structures except for a hydrogen bond between His^{71}-Gln^{192} (Fig. 2, D and E). At the C terminus, His^{193} shows extensive protein interactions in both open and closed conformations (Fig. 2, B to E), suggesting a potential role in conformational transition or structural integrity. This observation is also supported by the loss of function in individual mutants of His^{193} to Asn, Gln, Cys, Gly, or Arg (*26*). However, in a previous study, when the C-terminal four residues of *Hp*UreI (Gln-His-Trp-Val) were replaced by the last three residues (Gly-Lys-Trp) of its homolog *Ss*UreI, the mutant gave full activity and showed normal gating (*26*). This chimera showed that His^{193} cannot be a sensor for opening with a pK_a of ~6. Last, at the PL2 loop, the position of His^{131} in the closed and open conformations is markedly different, suggesting a possible role as the initiator of transition to the open conformation. The side chain of His^{131} faces outward in closed conformation and then switches to inward and forms a strong hydrogen bond with the side-chain oxygen of Glu^{138} in the open conformation (Fig. 2, D and E). Furthermore, Glu^{138} is also hydrogen-bonded to the backbone amide hydrogen of Val^{195}, which makes Glu^{138} an important intermediary that connects His^{131} and the C terminus together (Fig. 2E). It was also reported that any mutation of His^{131} or Glu^{138} causes loss of activity (*26*). These findings indicate that protonation of His^{131} in PL2 initiates conversion to the open conformation, where its interaction with Glu^{138} helps stabilize the orientation of the C terminus. Hence, His^{131} is the pH sensor for gating.

Closed-open conformational transition involves interprotomer cooperation

As noted above, PL1, PL2, and C terminus in the periplasmic domain show marked conformational changes in the two cryo-EM structures at pH 7.0 and 4.8, in contrast to the cytoplasmic half of the channel that shows little change. Superimposition of the closed and open cryo-EM structures for a single protomer identifies the moving segments of the protein backbone in PL1, PL2, and the C terminus (Fig. 2A, red arrows).

In the closed conformation, a segment of PL1, comprising the sequence (His^{70}-His^{71}-Leu^{72}-Thr^{73}) near the start of TM3, crosses over the periplasmic end of the channel and then moves to the outer edge of the channel in the open conformation (Fig. 2, B and C). Because of steric conflict (black triangle in Fig. 3, A and B), this reorientation of PL1 is not possible until the C terminus of the adjacent protomer moves away from the position it occupies in the closed channel. This is accomplished with a 180° flip of the last four residues at the C terminus, which, in turn, requires previous rearrangement of PL2 on the same protomer (movie S5). Therefore, the PL2 segment has to move before other segments, which is consistent with the transition trigger His^{131} located at PL2. In both closed and open conformations, there are extensive protein interactions stabilizing the PL1, PL2, and C termini conformations. In detail, in the closed conformation, Ser^{125} of PL2 forms a hydrogen bond with the backbone carbonyl oxygen of Val^{195} from the adjacent protomer and then switches to the side-chain oxygen of Ser^{69} in the open conformation. Gln^{192} also plays a key role by changing from interacting with Asp^{130} of its own PL2 in the closed conformation to stabilizing the open conformation of PL1 on the adjacent protomer via hydrogen bonding the backbone carbonyl oxygen of His^{71} (H71′ in Fig. 2E).

Therefore, the following hypothesis is proposed. Conversion to the open conformation requires a sequence of coordinated transitions (Fig. 3), beginning with the movement of PL2 to the periphery of the hexamer in one protomer (Fig. 3B, protomer A, step "I"), followed by a ~180° flip in the orientation of the C terminus (Fig. 3B, protomer A, step "II") and then the movement of PL1 of the adjacent channel (PL1′ of protomer F in Fig. 3B, step "III"). These stepwise, pH-driven movements involve cooperation between adjacent protomers. These cooperative movements are in closely balanced equilibrium, as shown by only a ~20-fold change in the rate of urea passage between pH 5.0 and 7.0, amounting to less than 3.0 kcal free energy difference between open and closed conformations (fig. S8A). This balance is predicted to be shifted in favor of the open conformation by protonation of His^{131} based on our structural results and on the pH midpoint for channel gating of ~6.0 for wild-type *Hp*UreI.

To further identify the specific residues involved in the conformational transition, we examined a series of mutants in PL1, PL2, and the C terminus (Fig. 2F and fig. S8C). Alanine mutants of certain hydroxyl-containing residues in either PL1 or PL2 showed increased open probabilities at pH 7.5, confirming their direct involvement in stabilizing the closed channel. Mutants Thr^{73}Ala and Ser^{74}Ala near the end of PL1 showed defective gating with 1.6- and 1.4-fold increases in activity at pH 5.0 and 9- and 6-fold increases at pH 7.5, respectively (Fig. 2, D to F), compared to unmutated 6his*Hp*UreI. Thr^{73} and Ser^{74} therefore help stabilize the closed conformation, and loss of their side-chain interactions in the mutants favors the open channel. The increased activity in these mutants implies that the observed orientation of PL1 in the closed conformation is inhibitory and that a significant fraction of the protomers remain closed in the unmutated channel at pH 5.0. Similarly, mutants Ser^{122}Ala and Ser^{125}Ala showed 10- and 11-fold activation of urea passage, respectively, at pH 7.5, indicating greater stabilization of the closed conformation versus the open conformation of PL2 by these serines (Fig. 2, D to F). The increased activity at pH 7.5 shows that the probability of channel opening is not entirely determined by protonation of His^{131} in these mutants and that mutations in PL1 or PL2 can favor the open channel, emphasizing that the conformational states of PL1, PL2, and the C terminus are in equilibrium and interdependent.

Evolution of the expanded PLs unique to UreI is in keeping with the development of the gating mechanism. However, many of the

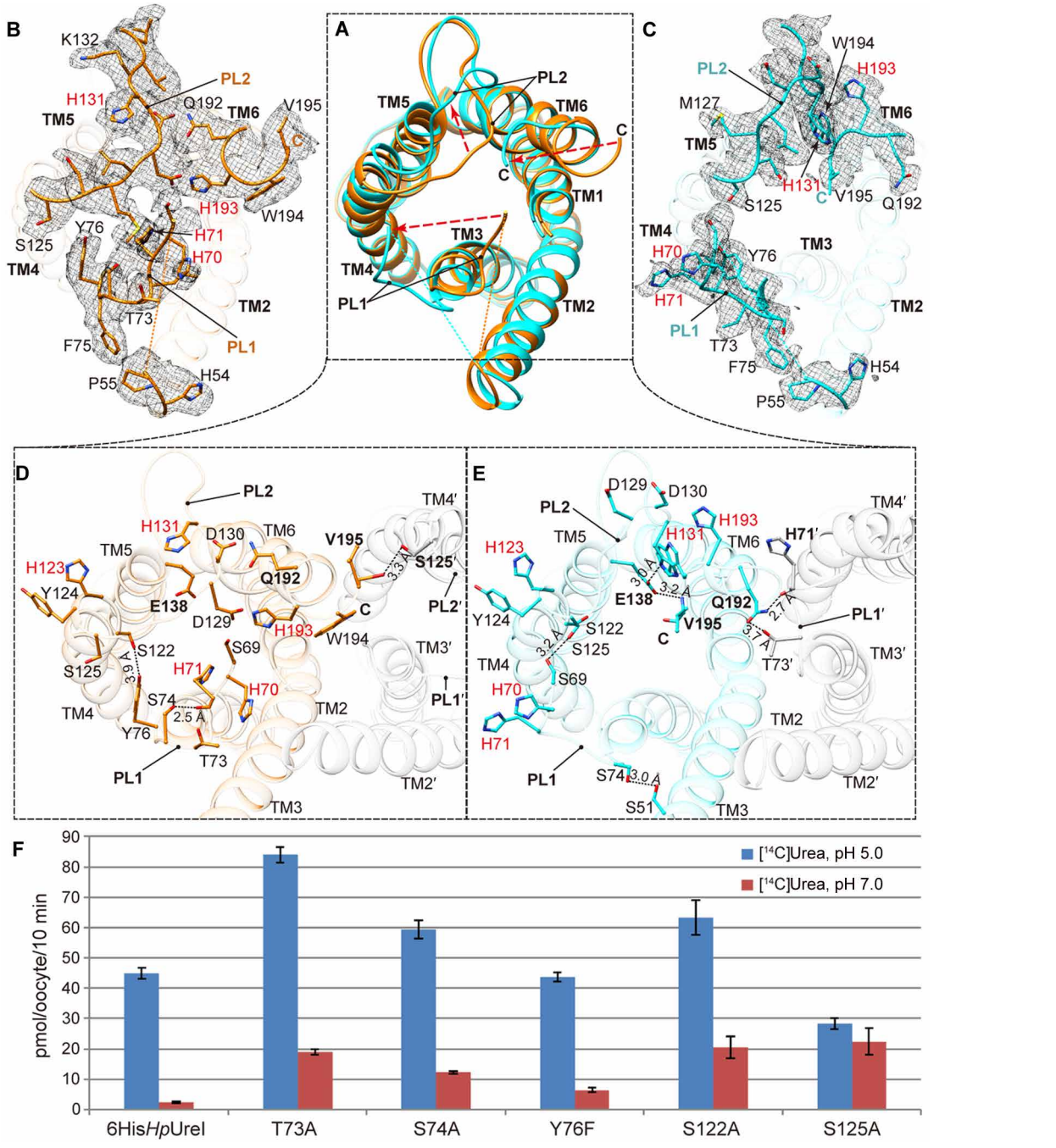

Fig. 2. Comparison of PLs and C terminus in the closed and open conformations. (**A**) Overlaid protomers (ribbons) in closed (orange) and open (cyan) conformations, as viewed from the periplasm. Conformational changes are marked by red arrows. (**B** and **C**) Cryo-EM density of PL1, PL2, and C terminus in either the closed (B) or open (C) conformation, overlaid with the atomic model of a protomer of each conformation. (**D** and **E**) Key residues and interactions involved in conformation transition in closed (orange) and open (cyan) conformations. The neighboring protomers are in gray. (**F**) [^{14}C]Urea influx (pmol/oocyte per 10 min) for oocytes expressing point mutants of 6his*Hp*UreI as compared to the control.

residues at the interprotomer interfaces are highly conserved in the AmiS family, and we sought to determine whether this interface is also important for function. Trp^{183} and Trp^{187} form a large part of the surface between protomers at the periplasmic end of TM6. Therefore, mutants Trp^{183}Ala and Trp^{187}Ala were expressed and found to be inactive (fig. S8C), suggesting that a stable interprotomer interface is important for conformational transition or stability.

Shape and length of the channel pore determine the rate of urea passage

The conformational changes in the PLs and the C terminus occur concurrently with shifts in the membrane helices (TMs) as part of channel opening. These changes in the periplasmic part of the TMs are illustrated by overlaying single protomers in their closed and open conformations (Fig. 4A). Shifts in the TMs, in turn, affect the

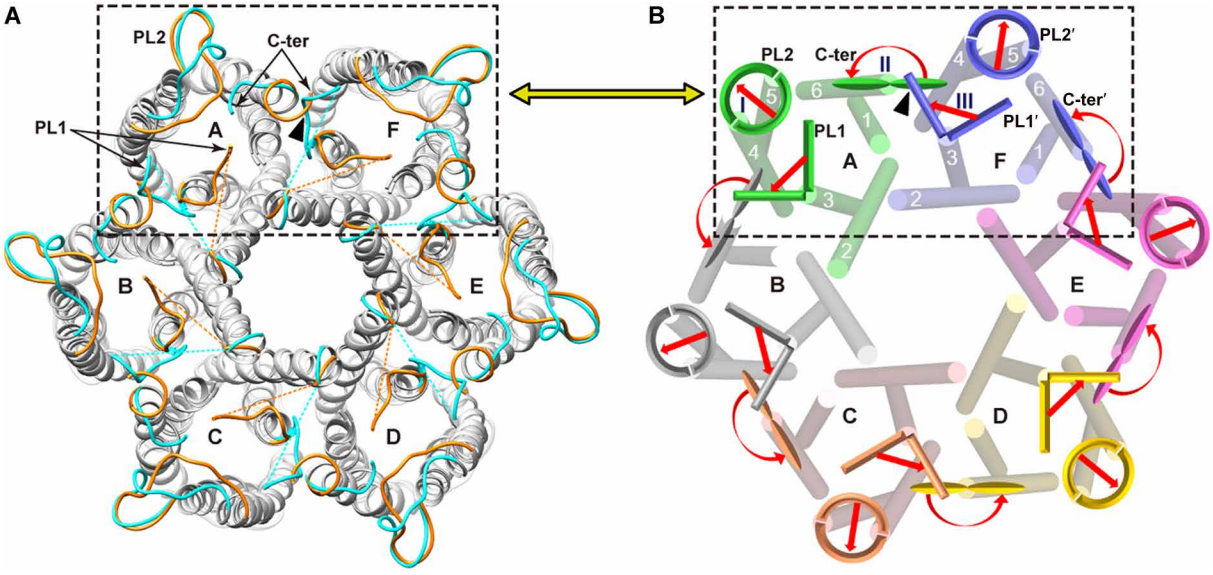

Fig. 3. Comparison of closed and open conformations of 6his*Hp*UreI elucidates coordinated transitions involving interprotomer cooperation. (**A**) Periplasmic view of superposed hexamers in closed and open conformations, with their PL1, PL2, and C terminus highlighted in orange (closed) and cyan (open). (**B**) Illustration of sequential cooperative changes in one protomer (A) that would convert a neighboring protomer (F) from closed to open conformation (black dashed boxes). Our structures show that steric hindrance (black triangle) would prevent the simultaneous occurrence of the C terminus (C-ter) of protomer A in its closed conformation and PL1′ of protomer F in its open conformation. We posit that, as indicated by arrows, the movement of PL2 on protomer A (step I) allows its C terminus to flip 180° (step II), which makes space for PL1′ of the neighboring protomer F to reorient to the open conformation (step III). The final open state of protomer F (i.e., the open channel structure presented here) would then be formed with conversion of its own PL2 (PL2′) and C terminus (C-ter′) to the open conformation.

orientations of side chains lining the channel pore that define the urea pathway (dots in Fig. 4, B and C). These evidently increase the rate of urea transit to the cytoplasm by increasing urea access to the filter near the middle of the membrane and by slightly changing the shape of the filter itself (Fig. 4, B to E).

Especially clear changes are found for the aromatic side chains, where the movement of PL2 is associated with a shift in TM4 and TM5 by more than 1.0 Å, which alters the orientation of Trp^{142}, Trp^{146}, Trp^{149}, and Trp^{153} (Fig. 4, A, D, and E). Mutation of these residues caused severe loss of activity (Fig. 4G). PL1 movement to the periphery correlates with an outward shift of TM3, significantly expanding the pore near Trp^{142} in the open conformation (compare green and purple dots in Fig. 4, B and C, respectively). In contrast, PL1 crosses the middle of the channel at its periplasmic end in the closed conformation, constricting the pore and increasing its length (red dots at the top of Fig. 4B). The path through the pore near the urea filter is somewhat longer and narrower in the closed conformation (red dots next to Trp^{153} in Fig. 4B) than in the open channel (Fig. 4C). The filter region is nevertheless too narrow and short for urea passage even in the open conformation, suggesting that side-chain reorientations of Trp^{153}, Leu^{13}, and Tyr^{88} (and possibly Trp^{149}) would be necessary for urea to transit the filter, as suggested by molecular dynamics simulations using the 6his*Hp*UreI crystal structure (*27*). Small changes in the side-chain orientations for these residues, identified by using the program HADDOCK2.2 (*28*), allowed urea to fit in the filter (fig. S9). The largest change was seen for Trp^{153} with a flip in the plane of the side chain by ~60° (fig. S9B). In contrast to the other tryptophans in the channel, mutation of Trp^{153} did not inhibit the rate of urea transit but eliminated selectivity for urea as compared to thiourea (*15*). These observations are consistent with the proposed tight fit of urea in the filter next to Trp^{153} and suggest that even the small changes in the geometry of the filter observed in the closed conformation may slow urea passage. In the closed conformation, the overall pore is lengthened by the movement of PL1, PL2, and the C terminus (Fig. 4B), and urea entry into the pore at the periplasmic end appears restricted by its small diameter. These observed changes are proposed to be sufficient to decrease urea passage to the cytoplasm by the relatively small factor found in the oocyte expression assay (~20-fold; Fig. 4F) and suggest that impaired diffusion of urea from the periplasmic end of the pore through the filter is the primary cause of decreased urea throughput in the closed conformation.

To identify the key residues inside the urea channel, we designed a series of mutants and analyzed their [^{14}C]urea transit activities in oocytes. Residues defining the overall urea pathway can be categorized as contributing either to the entry path approaching the urea filter, the filter itself next to Trp^{153}, or the exit path to the cytoplasm. Our mutational analyses in these sections of the channel revealed the functional importance of aliphatic residues Leu^{2}, Val^{5}, and Leu^{6} in TM1, as part of the urea entry path (Fig. 4, B, C, and F). Mutating aromatic residues that line the approach to the filter including Trp^{141}, Trp^{142}, Trp^{146}, Trp^{149}, Phe^{84} (*15*), and Tyr^{88} also resulted in significant loss of activity (Fig. 4, D, E, and G, and fig. S8C), indicating that their side chains play important roles in urea passage. Furthermore, mutants of residues in or near the urea filter, such as Leu^{13}Ala, Tyr^{88}Ser, Leu^{152}Ala, and Thr^{87}Ala, lost activity (Fig. 4F and fig. S8C). These results support the strict structural requirements for urea passage through the filter. Mutation of Glu^{177} to leucine next to the urea filter was strongly deactivating, suggesting a possible role for this residue in orienting urea in

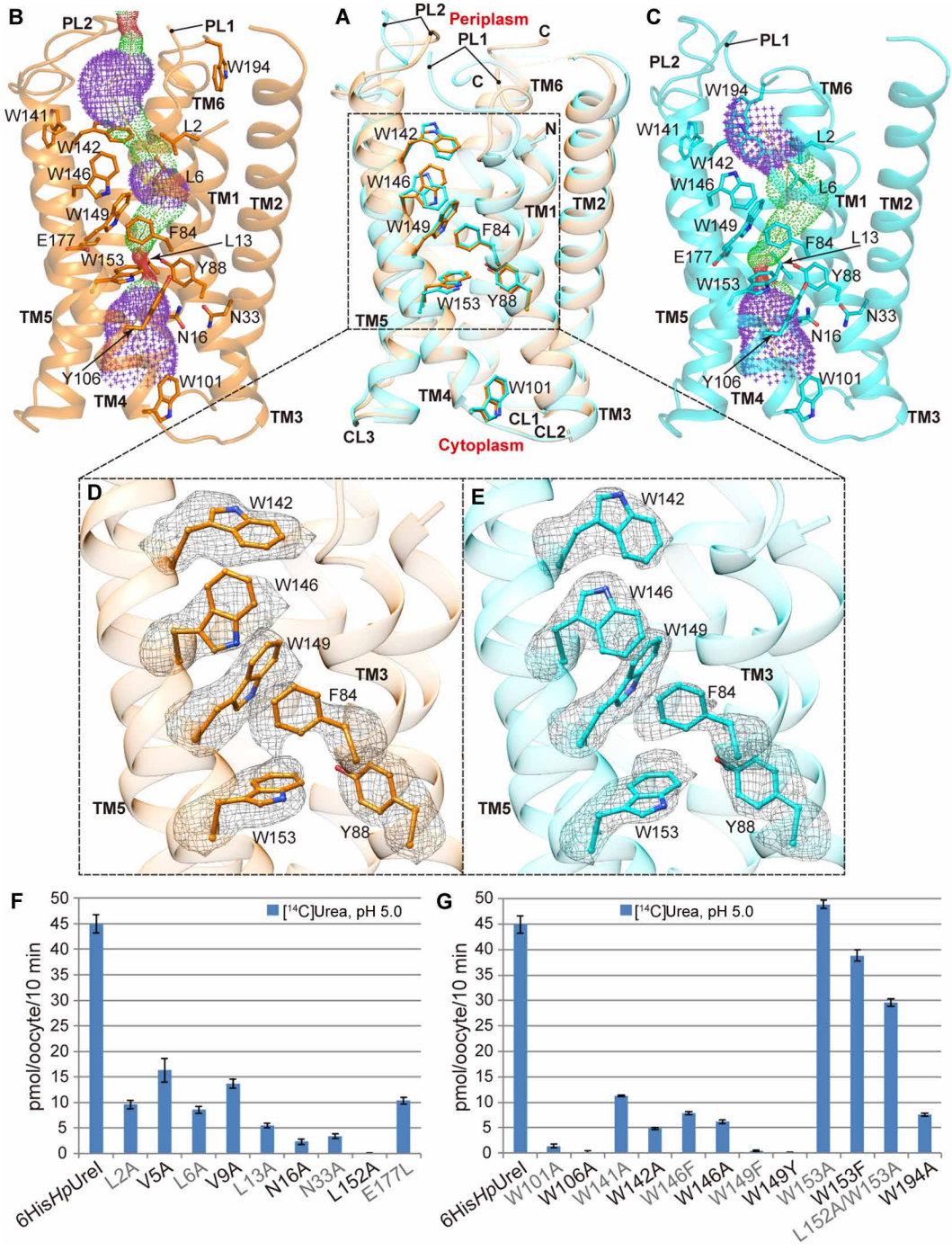

Fig. 4. Change in the solvent accessibility of the channel between closed and open conformations and significances of the residues lining the channel. (**A**) Superposition of the channel in the closed (orange) and open (cyan) conformations. (**B** and **C**) The solvent accessibilities of the channel as determined by HOLE program in the closed (B) and open (C) conformations (dots). Red for pore radii < 1.2 Å, green for 1.2 Å < pore radii < 2.3 Å, and purple for 2.3 Å < pore radii < 4.0 Å. (**D** and **E**) Aromatic residues, particularly tryptophans, lining the channel. The side chains of these residues are well defined in the cryo-EM map (mesh). (**F**) [^{14}C]Urea influx (pmol/oocyte per 10 min) for oocytes expressing mutants of 6his*Hp*Urel. (**G**) [^{14}C]Urea influx (pmol/oocyte per 10 min) for oocytes expressing tryptophan mutants of 6his*Hp*Urel. Comparison to the control shows significant loss of activity for point mutation replacing channel-lining Trp^{141}, Trp^{142}, Trp^{146}, or Trp^{149}.

the filter (Fig. 4F). On the cytoplasmic side of the urea channel, mutation of two highly conserved asparagines (Asn^{16} and Asn^{33}) to alanine was inactivating, and they are suggested to play a key role in urea exit to the cytoplasm (Fig. 4F). In summary, mutation of residues that line the channel results in loss of activity, suggesting that a complex network of side chains controls the shape of the pore and urea diffusion through the channel and specificity filter.

SUMMARY AND CONCLUSIONS

In summary, we have determined the structures of the closed and open conformations of *H. pylori* UreI channel both at a resolution of 2.7 Å. Comparison of these conformations and systematic activity analyses of mutants point to a gating mechanism of *Hp*UreI involving pH sensing, interprotomer cooperation and modification of the urea pathway. In this mechanism, driven by pH change, His^{131} on PL2 triggers the sequential and cooperative movements of PL1, PL2, and the C terminus in the periplasmic domain. These changes in the periplasmic domain are further associated with displacement of the transmembrane helices accompanied by reorientation of side chains lining the channel interior. All of these conformational transitions exist in closely balanced equilibrium to shift both the shape and length of the channel in favor of urea passage at low pH in support of *H. pylori* survival in a hostile acidic environment. Targeting residues that define the shape of the channel, especially in the approach to the urea filter in the open conformation, represents a starting point for the rational design of novel *Hp*UreI inhibitors.

MATERIALS AND METHODS

Purification of 6his*Hp*UreI and sample optimization for cryo-EM

The 6his-tagged protein was engineered as previously described (*15*). *Escherichia coli* C43 transformed with the pET101UreI6HIsPL1 plasmid and expressing 6his*Hp*UreI was grown in a BioFlo 110 (New Brunswick) bioreactor, the cells were collected and passed through a French press at 20,000 psi in the presence of deoxyribonuclease, and membranes were prepared by differential centrifugation as described in detail previously (*15*). Membranes at a protein concentration of 10 mg/ml were suspended in degassed resuspension buffer [RB; 10 mM imidazole, 150 mM NaCl, and 50 mM Na_2HPO_4 (pH 7.4)], treated with decylmaltoside (DM; Anatrace Inc.) at a final concentration of 2% for 45 min at 4°C, and centrifuged (33,000 rpm for 30 min at 4°C). TALON cobalt resin (5 ml; Clontech) was added to the supernatant, and the solution was rotated for 4 hours at 4°C. The resin was rinsed in a small column with 50 ml of RB containing 10 mM imidazole and 0.2% DM and then with 150 ml of RB containing 20 mM imidazole and 0.2% DM. 6his*Hp*UreI was eluted from the resin with RB containing 200 mM imidazole and 0.2% DM and concentrated to 1.5 ml using a centrifugal filter (Amicon Ultra, 50-kDa cutoff) to a protein concentration of 2 mg/ml.

Sample evaluation and optimization were carried out with negative-stain transmission electron microscopy (TEM) in a TF20 (FEI) electron microscope. Briefly, an aliquot of 2.5 μl of the sample at 50 μg/ml 6his*Hp*UreI and 0.2% DM was applied to carbon-coated TEM grids (Ted Pella) and stained with 2% uranyl acetate. Particles in the negative-stain TEM micrographs appear uniform (fig. S10A), and the same sample at 1 mg/ml 6his*Hp*UreI gave optimized particle distribution on QUANTIFOIL 2/1 cryo-EM grids. Cryo-EM micrographs recorded in a Titan Krios high-resolution electron microscope from these grids showed excellent contrast of particles but produced 2D class averages without high-resolution features (fig. S10, B and C). Given that crystal structure was determined from 6his*Hp*UreI purified in the presence of 0.2% DM, we presume that the high contrast from DM might have overwhelmed that of 6his*Hp*UreI protein, preventing the computational alignment of the integral membrane proteins in different micrographs.

To overcome this problem, amphipol PMAL-C8 (Anatrace Inc.) was used to replace DM in the sample. A 0.3-ml RB solution containing 12 mg of PMAL-C8 (Anatrace Inc.) and 200 mM imidazole was added to the 1.5-ml protein solution at a concentration of 2 mg/ml. After overnight incubation at 4°C, 60 mg of Bio-Beads SM-2 (Bio-Rad) was added to remove unbound DM and PMAL-C8, and the solution was rotated for 3.5 hours. The Bio-Beads were removed by filtration (0.45-μm Ciro filter, Chrom Tech Inc.), the solution was concentrated with a centrifugal filter (Amicon Ultra, 50 kDa cutoff) to 0.35 ml, and the sample was passed over a column of Superose 6 using a buffer of 150 mM NaCl and 10 mM bis-tris (pH 7.0). A sample of 0.2 ml at the peak of Abs280 was collected and used directly for cryo-EM (see below) of the closed state without further treatment. The same procedure was used for the open-channel conformation, except that the gel filtration buffer was 150 mM NaCl, 10 mM bis-tris, and 1 mM Na acetate (pH 4.8). The pH of both closed and open channel samples was verified before freezing for cryo-EM.

Expression of 6his*Hp*UreI in oocytes and [^{14}C]urea influx

Site-specific mutants were encoded in the gene for 6his*Hp*UreI by using pET101UreI6HIsPL1 and the QuikChange method (Stratagene) with the appropriate primers. Capped and polyA-tailed RNAs [complementary RNA (cRNA)] were prepared with the mMESSAGE mMACHINE T7 Ultra Kit (Ambion). Oocytes (EcoCyte Bioscience US LLC) were injected with cRNA (50 nl of 1 μg/μl) and incubated for 2 days at 18°C in Barth's solution [88 mM NaCl, 2.4 mM $NaHCO_3$, 1 mM KCl, 0.4 mM $CaCl_2$, 0.3 mM $Ca(NO_3)_2$, 0.8 mM $MgSO_4$, and 10 mM Hepes-tris (pH 7.5)]. Oocytes were then washed twice (1.0 ml) with Ringer's solution (100 mM NaCl, 2 mM KCl, 1 mM $CaCl_2$ and $MgCl_2$, and 20 mM MES at pH 5.0), transferred into 0.5 ml of the same buffer, and incubated at 22°C for 10 min in the presence of 100 μM [^{14}C]urea to measure urea influx into the oocytes for the open channel. The buffer pH was adjusted to the values indicated on the graphs for measuring urea influx as a function of pH. MES was changed to Hepes when pH 7.5 was required. Oocytes (6 to 10 per data point) were washed twice with 10 volumes of ice-cold Barth's solution to terminate 100 μM [^{14}C]urea influx and then dissolved in 10% SDS and counted after addition of 5.0 ml of Hionic-Fluor scintillant. Error bars show SEM for each set of oocytes. Several (three to six) injected oocytes were saved for each mutant and dissolved in 0.1 M NaCl, 0.02 M tris-HCl (pH 7.6), and 1% Triton (50 μl per oocyte). After centrifugation at 14,000 rpm for 5 min, 20 μl of the supernatant was separated by SDS–polyacrylamide gel electrophoresis, and the gels were transferred onto nitrocellulose, treated with an *Hp*UreI antibody generated against PL1 (CEGAEDIAQVSHHLTSFYGPATG), and developed by using an alkaline phosphatase (Promega)–tagged secondary antibody. All mutants were expressed at or above the level of 6his*Hp*UreI within an estimated error of ±20% based on densitometry scans.

Cryo–electron microscopy

An aliquot of 2.5 μl of purified 6his*Hp*UreI sample at a concentration of approximately 2 mg/ml was applied to a QUANTIFOIL holey carbon grid (2/1, 300 mesh), which was glow-discharged for 20 s with a PELCO easiGlow system. The grid was blotted and plunge-frozen in liquid ethane with Vitrobot IV at 4°C under 100% humidity. The frozen grids were stored in liquid nitrogen before use.

Frozen-hydrated cryo-EM grids were loaded into an FEI Titan Krios electron microscope operated at 300 kV, equipped with Gatan Quantum imaging filter (GIF) and a post-GIF K2 Summit direct electron detector. Movies were recorded as dose-fractionated frames in super-resolution mode with Legion3.1 (*29*) at a nominal magnification of ×130,000, corresponding to a calibrated pixel size of 0.535 Å on the specimen. The slit width in the GIF system was set to 20 eV to remove inelastically scattered electrons. For the dataset of the closed conformation, the dose rate on the camera was set to 1.4 electrons/pixel per second, corresponding to 4.8 electrons/Å^2 per second. An exposure time of 15 s was used at a rate of 0.15 s/frame, giving rise to 100 frames and a total dosage of 72 electrons/Å^2 for each movie. For the dataset of the open conformation, the dosage and frame rates were the same as those used for the closed conformation, but the exposure time was set to 9 s, giving rise to 60 frames and a total dosage of 43 electrons/Å^2 for each movie. A total of 5505 and 3140 movies were recorded for the closed and open conformations, respectively. Details of the experimental conditions are summarized in table S1.

Data processing

All but the first and last frames in each movie were motion-corrected with a subframe 5 × 5 to generate two motion-corrected micrographs (with and without dose weighting), which were both binned 2 × 2 to yield a pixel size of 1.07 Å with MotionCor2 (*30*). The micrographs without dose weighting were used for contrast transfer function (CTF) determination with ctffind4.1.18 (*31*) and for particle picking with Gautomatch (*32*). To reduce aliasing because of the CTF oscillation at high frequency, the micrographs with dose weighting were corrected for CTF by phase flipping using Bsoft (*33*) before particle extraction.

Data processing workflows for the closed and open states are essentially the same, as detailed in figs. S6 and S7, respectively. For the dataset of the closed conformation, 4026 micrographs were selected by manual screening to discard those either with underfocus values greater than 3.0 μm, or with very few particles, or containing crystalline ice. A total of 1,221,897 particles were extracted from these selected micrographs using RELION (*34*, *35*). These particles were subjected to 3D classification in RELION with C6 symmetry. The initial reference used for this step was a simple binary (0s and 1s) cylinder of radius 45 Å and height 45 Å generated by EMAN2 (*36*) and low pass–filtered to a resolution of 60 Å. This 3D classification was used to sort particles into three classes with 5 pixels and 3.8° as the translation and rotation search parameters, respectively. Thirty-eight percent of the particles went to a class (the "good" class) with clear visible features of α helices (fig. S6). The particles in this good class were then subjected to reference-free 2D classification by requesting 200 classes, and then 393,930 particles from 61 featured class averages were selected (fig. S1B). Subsequently, these particles were subjected to another round of 3D classification by requesting three classes, which were further autorefined separately, yielding three 3D maps at resolutions of 3.2, 3.4, and 3.3 Å. Because these maps appeared identical, all these particles were combined in a 3D autorefinement, yielding a map at a resolution of 3.1 Å. The resolution of the final map was improved to 2.7 Å, by using focus alignment with a tighter mask created by removing the amphipol density (fig. S6).

For the open dataset, 1,017,209 particles were extracted from 2901 good micrographs. After first-round 3D and 2D classifications, 343,366 particles were selected from good classes. Subsequently, these particles were subjected to another round of 3D classification by requesting three classes, from which two good classes were further autorefined separately, yielding two 3D maps at resolutions of 3.2 and 3.4 Å. Particles (279,840) from these two classes were combined in a 3D autorefinement, yielding a map at a resolution of 3.0 Å. The resolution of the final map was improved to 2.7 Å, by using focus alignment with a tighter mask created by removing the amphipol density (fig. S7).

All resolutions reported above are based on the "gold standard" refinement procedures and the 0.143 Fourier shell correlation criterion. Local resolution was estimated using MonoRes (*37*).

Model building

Atomic model building was accomplished with Coot (*38*). Briefly, while the cryo-EM density would allow atomic model building de novo in this case, the crystal structure of *Hp*UreI containing a 6his tag in PL1 [Protein Data Bank (PDB), 3UX4] was fitted into the cryo-EM maps (with mask) of the closed and open channels, respectively, as initial models by using the "fit-in map" routine in Chimera (*39*). The crystal structure, however, was poorly fit to the cryo-EM maps in many places, and the models required extensive manual building. In the periplasmic domain, PL1 required addition of residues missing in the crystal structure, and PL2 and the four residues at the C terminus were fit poorly. Although 13 residues in PL1, Thr^{56}-Val^{68}, could not be seen in the cryo-EM density maps or the crystal structure, a critical segment of PL1 from Ser^{69}-Thr^{73} not in the crystal structure was present in both closed and open maps. These five residues were added and refined for each conformation. PL2 and the C terminus of the crystal structure did not match the cryo-EM density maps and had to be completely rebuilt. The structures were then refined in real space using "real-space refinement" in Phenix (*40*) until the peptide backbone dihedrals and side-chain conformations were optimized. Ramachandran, secondary structure, and noncrystallographic symmetry restraints were used for setting up the Phenix refinement. MolProbity (*41*) was used to validate the stereochemistry of the final models. The final refinement statistics for both closed and open conformational models are summarized in table S1.

The cryo-EM maps and atomic models were visualized using UCSF Chimera (*39*) or PyMOL (*42*). HOLE (*43*) was used to calculate the pore profile shown in Fig. 4 (B and C). HADDOCK2.2 (*28*) was used to fit urea in the filter.

SUPPLEMENTARY MATERIALS

Supplementary material for this article is available at http://advances.sciencemag.org/cgi/content/full/5/3/eaav8423/DC1

Fig. S1. Cryo-EM analysis of 6his*Hp*UreI in closed conformation.
Fig. S2. Cryo-EM analysis of 6his*Hp*UreI in open conformation.
Fig. S3. Cryo-EM densities (mesh) of the six TM helices in 6his*Hp*UreI in the closed and open conformations superposed with their atomic models.
Fig. S4. Details of the cryo-EM densities overlaid with their atomic models (sticks) of the PLs and C terminus in the closed (orange) and open (cyan) conformations.
Fig. S5. Ordered lipids resolved in the cryoEM density maps.
Fig. S6. Data processing workflow used for the dataset recorded for the sample in the closed conformation.
Fig. S7. Data processing workflow used for the dataset recorded for the sample in the open conformation.
Fig. S8. Urea passage activity for wild-type *Hp*UreI and mutants of 6his*Hp*UreI.
Fig. S9. Proposed filter model for urea fitted in the open conformation of 6his*Hp*UreI by using HADDOCK2.2.

Fig. S10. Sample quality evaluation for 6his*Hp*UreI in DDM other than amphipol.
Table S1. Statistics of the cryo-EM structures.
Movie S1. Cryo-EM density views of 6his*Hp*UreI in closed conformation.
Movie S2. Atomic model and density fit views of 6his*Hp*UreI in closed conformation.
Movie S3. Cryo-EM density views of 6his*Hp*UreI in open conformation.
Movie S4. Atomic model and density fit views of 6his*Hp*UreI in open conformation.
Movie S5. 6his*Hp*UreI closed and open conformations morph.

REFERENCES AND NOTES

1. J. K. Y. Hooi, W. Y. Lai, W. K. Ng, M. M. Y. Suen, F. E. Underwood, D. Tanyingoh, P. Malfertheiner, D. Y. Graham, V. W. S. Wong, J. C. Y. Wu, F. K. L. Chan, J. J. Y. Sung, G. G. Kaplan, S. C. Ng, Global prevalence of *Helicobacter pylori* infection: Systematic review and meta-analysis. *Gastroenterology* **153**, 420–429 (2017).
2. V. Cherezov, D. M. Rosenbaum, M. A. Hanson, S. G. F. Rasmussen, F. S. Thian, T. S. Kobilka, H.-J. Choi, P. Kuhn, W. I. Weis, B. K. Kobilka, R. C. Stevens, High-resolution crystal structure of an engineered human β_2-adrenergic G protein-coupled receptor. *Science* **318**, 1258–1265 (2007).
3. V. Herrera, J. Parsonnet, *Helicobacter pylori* and gastric adenocarcinoma. *Clin. Microbiol. Infect.* **15**, 971–976 (2009).
4. D. H. Jung, J.-H. Kim, Y. C. Lee, S. K. Lee, S. K. Shin, J. C. Park, H. S. Chung, H. Kim, H. Kim, Y. H. Kim, J. J. Park, Y. H. Youn, H. Park, *Helicobacter pylori* eradication reduces the metachronous recurrence of gastric neoplasms by attenuating the precancerous process. *J. Gastric Cancer* **15**, 246–255 (2015).
5. I. J. Choi, M.-C. Kook, Y.-I. Kim, S.-J. Cho, J. Y. Lee, C. G. Kim, B. Park, B.-H. Nam, *Helicobacter pylori* therapy for the prevention of metachronous gastric cancer. *N. Engl. J. Med.* **378**, 1085–1095 (2018).
6. M. Rugge, R. M. Genta, F. Di Mario, E. M. El-Omar, H. B. El-Serag, M. Fassan, R. H. Hunt, E. J. Kuipers, P. Malfertheiner, K. Sugano, D. Y. Graham, Gastric cancer as preventable disease. *Clin. Gastroenterol. Hepatol.* **15**, 1833–1843 (2017).
7. D. Y. Graham, History of *Helicobacter pylori*, duodenal ulcer, gastric ulcer and gastric cancer. *World J. Gastroenterol.* **20**, 5191–5204 (2014).
8. J. Houghton, T. C. Wang, *Helicobacter pylori* and gastric cancer: A new paradigm for inflammation-associated epithelial cancers. *Gastroenterology* **128**, 1567–1578 (2005).
9. D. S. Merrell, M. L. Goodrich, G. Otto, L. S. Tompkins, S. Falkow, pH-regulated gene expression of the gastric pathogen *Helicobacter pylori*. *Infect. Immun.* **71**, 3529–3539 (2003).
10. B. N. Dang, D. Y. Graham, *Helicobacter pylori* infection and antibiotic resistance: A WHO high priority? *Nat. Rev. Gastroenterol. Hepatol.* **14**, 383–384 (2017).
11. H. L. Mobley, M. D. Island, R. P. Hausinger, Molecular biology of microbial ureases. *Microbiol. Rev.* **59**, 451–480 (1995).
12. D. L. Weeks, S. Eskandari, D. R. Scott, G. Sachs, A H^+-gated urea channel: The link between *Helicobacter pylori* urease and gastric colonization. *Science* **287**, 482–485 (2000).
13. L. R. Gray, S. X. Gu, M. Quick, S. Khademi, Transport kinetics and selectivity of *Hp*UreI, the urea channel from *Helicobacter pylori*. *Biochemistry* **50**, 8656–8663 (2011).
14. D. L. Weeks, G. Gushansky, D. R. Scott, G. Sachs, Mechanism of proton gating of a urea channel. *J. Biol. Chem.* **279**, 9944–9950 (2004).
15. D. Strugatsky, R. McNulty, K. Munson, C.-K. Chen, S. M. Soltis, G. Sachs, H. Luecke, Structure of the proton-gated urea channel from the gastric pathogen *Helicobacter pylori*. *Nature* **493**, 255–258 (2013).
16. S. A. Wilson, R. J. Williams, L. H. Pearl, R. E. Drew, Identification of two new genes in the *Pseudomonasaeruginosa* amidase operon, encoding an ATPase (AmiB) and a putative integral membrane protein (AmiS). *J. Biol. Chem.* **270**, 18818–18824 (1995).
17. G. H. M. Huysmans, N. Chan, J. M. Baldwin, V. L. G. Postis, S. B. Tzokov, S. E. Deacon, S. Y. M. Yao, J. D. Young, M. J. McPherson, P. A. Bullough, S. A. Baldwin, A urea channel from *Bacillus cereus* reveals a novel hexameric structure. *Biochem. J.* **445**, 157–166 (2012).
18. G. Sachs, D. L. Weeks, K. Melchers, D. R. Scott, The gastric biology of *Helicobacter pylori*. *Annu. Rev. Physiol.* **65**, 349–369 (2003).
19. K. W. Huynh, J. Jiang, N. Abuladze, K. Tsirulnikov, L. Kao, X. Shao, D. Newman, R. Azimov, A. Pushkin, Z. H. Zhou, I. Kurtz, CryoEM structure of the human SLC4A4 sodium-coupled acid-base transporter NBCe1. *Nat. Commun.* **9**, 900 (2018).
20. Z. Zhang, F. Liu, J. Chen, Conformational changes of CFTR upon phosphorylation and ATP binding. *Cell* **170**, 483–491.e8 (2017).
21. J. Jiang, B. L. Pentelute, R. J. Collier, Z. H. Zhou, Atomic structure of anthrax protective antigen pore elucidates toxin translocation. *Nature* **521**, 545–549 (2015).
22. Y. Kang, O. Kuybeda, P. W. de Waal, S. Mukherjee, N. van Eps, P. Dutka, X. E. Zhou, A. Bartesaghi, S. Erramilli, T. Morizumi, X. Gu, Y. Yin, P. Liu, Y. Jiang, X. Meng, G. Zhao, K. Melcher, O. P. Ernst, A. A. Kossiakoff, S. Subramaniam, H. E. Xu, Cryo-EM structure of human rhodopsin bound to an inhibitory G protein. *Nature* **558**, 553–558 (2018).
23. J. R. Meyerson, S. Chittori, A. Merk, P. Rao, T. H. Han, M. Serpe, M. L. Mayer, S. Subramaniam, Structural basis of kainate subtype glutamate receptor desensitization. *Nature* **537**, 567–571 (2016).
24. M. Liao, E. Cao, D. Julius, Y. Cheng, Structure of the TRPV1 ion channel determined by electron cryo-microscopy. *Nature* **504**, 107–112 (2013).
25. W. Mi, Y. Li, S. H. Yoon, R. K. Ernst, T. Walz, M. Liao, Structural basis of MsbA-mediated lipopolysaccharide transport. *Nature* **549**, 233–237 (2017).
26. D. L. Weeks, G. Sachs, Sites of pH regulation of the urea channel of *Helicobacter pylori*. *Mol. Microbiol.* **40**, 1249–1259 (2001).
27. R. McNulty, J. P. Ulmschneider, H. Luecke, M. B. Ulmschneider, Mechanisms of molecular transport through the urea channel of *Helicobacter pylori*. *Nat. Commun.* **4**, 2900 (2013).
28. G. C. P. van Zundert, J. P. G. L. M. Rodrigues, M. Trellet, C. Schmitz, P. L. Kastritis, E. Karaca, A. S. J. Melquiond, M. van Dijk, S. J. de Vries, A. M. J. J. Bonvin, The HADDOCK2.2 Web Server: User-friendly integrative modeling of biomolecular complexes. *J. Mol. Biol.* **428**, 720–725 (2016).
29. C. Suloway, J. Pulokas, D. Fellmann, A. Cheng, F. Guerra, J. Quispe, S. Stagg, C. S. Potter, B. Carragher, Automated molecular microscopy: The new Leginon system. *J. Struct. Biol.* **151**, 41–60 (2005).
30. S. Q. Zheng, E. Palovcak, J.-P. Armache, K. A. Verba, Y. Cheng, D. A. Agard, MotionCor2: Anisotropic correction of beam-induced motion for improved cryo-electron microscopy. *Nat. Methods* **14**, 331–332 (2017).
31. A. Rohou, N. Grigorieff, CTFFIND4: Fast and accurate defocus estimation from electron micrographs. *J. Struct. Biol.* **192**, 216–221 (2015).
32. K. Zhang, Gautomatch: A GPU accelerated program for accurate, fast, flexible and fully automatic particle picking from cryo-EM micrographs with or without templates; https://www.mrc-lmb.cam.ac.uk/kzhang/.
33. J. B. Heymann, Bsoft: Image and molecular processing in electron microscopy. *J. Struct. Biol.* **133**, 156–169 (2001).
34. S. H. W. Scheres, RELION: Implementation of a Bayesian approach to cryo-EM structure determination. *J. Struct. Biol.* **180**, 519–530 (2012).
35. S. H. W. Scheres, A Bayesian view on cryo-EM structure determination. *J. Mol. Biol.* **415**, 406–418 (2012).
36. G. Tang, L. Peng, P. R. Baldwin, D. S. Mann, W. Jiang, I. Rees, S. J. Ludtke, EMAN2: An extensible image processing suite for electron microscopy. *J. Struct. Biol.* **157**, 38–46 (2007).
37. J. L. Vilas, J. Gómez-Blanco, P. Conesa, R. Melero, J. M. de la Rosa-Trevín, J. Otón, J. Cuenca, R. Marabini, J. M. Carazo, J. Vargas, C. O. S. Sorzano, MonoRes: Automatic and accurate estimation of local resolution for electron microscopy maps. *Structure* **26**, 337–344.e4 (2018).
38. P. Emsley, K. Cowtan, *Coot*: Model-building tools for molecular graphics. *Acta Crystallogr. D Biol. Crystallogr.* **60**, 2126–2132 (2004).
39. E. F. Pettersen, T. D. Goddard, C. C. Huang, G. S. Couch, D. M. Greenblatt, E. C. Meng, T. E. Ferrin, UCSF Chimera—A visualization system for exploratory research and analysis. *J. Comput. Chem.* **25**, 1605–1612 (2004).
40. P. D. Adams, P. V. Afonine, G. Bunkóczi, V. B. Chen, I. W. Davis, N. Echols, J. J. Headd, L.-W. Hung, G. J. Kapral, R. W. Grosse-Kunstleve, A. J. McCoy, N. W. Moriarty, R. Oeffner, R. J. Read, D. C. Richardson, J. S. Richardson, T. C. Terwilliger, P. H. Zwart, PHENIX: A comprehensive Python-based system for macromolecular structure solution. *Acta Crystallogr. D Biol. Crystallogr.* **66**, 213–221 (2010).
41. V. B. Chen, W. B. Arendall III, J. J. Headd, D. A. Keedy, R. M. Immormino, G. J. Kapral, L. W. Murray, J. S. Richardson, D. C. Richardson, *MolProbity*: All-atom structure validation for macromolecular crystallography. *Acta Crystallogr. D Biol. Crystallogr.* **66**, 12–21 (2010).
42. L. Schrödinger, The PyMOL molecular graphics system, version 1.7.2 (2014).
43. O. S. Smart, J. G. Neduvelil, X. Wang, B. A. Wallace, M. S. P. Sansom, HOLE: A program for the analysis of the pore dimensions of ion channel structural models. *J. Mol. Graph.* **14**, 354–360 (1996).

Acknowledgments: We thank K. Wang for the advice regarding amphipol, I. Atanasov and W. Hui for cryo-EM assistance, and J. Jiang for suggestions on data processing. **Funding:** This work was supported mainly by the NSF under grant no. DMR-1548924 and, in part, by grants from the NIH (R01GM071940/AI094386/DE025567 to Z.H.Z. and R01DK46917/DK53462/DK58333 to G.S.) and a GWLAHS VA merit award (to G.S.). We acknowledge the use of instruments in the Electron Imaging Center for Nanomachines supported by UCLA and grants from the NIH (S10RR23057, S10OD018111, and U24GM116792) and NSF (DBI-1338135). K.Z. acknowledges support from the China Scholarship Council. **Author contributions:** Z.H.Z., K.M., and G.S. conceived the project; K.M. engineered and isolated samples and performed functional analyses; Y.W. prepared cRNA; D.S. performed functional analyses; Y.C. evaluated the samples, performed electron microscopy, and processed the data; K.Z. built atomic models

and prepared figures with assistance from Y.C. and K.M.; Z.H.Z. supervised the cryo-EM studies. K.M., K.Z., and Z.H.Z. wrote the manuscript; all authors edited and approved the manuscript. **Competing interests:** The authors declare that they have no competing interests. **Data and materials availability:** All data needed to evaluate the conclusions in the paper are present in the paper and/or the Supplementary Materials. Additional data related to this paper may be requested from the authors. Coordinates and cryo-EM density maps are available at the PDB and the Electron Microscopy Data Bank under accession numbers PDB 6NSJ, PDB 6NSK, EMD-0498, and EMD-0499.

Submitted 24 October 2018
Accepted 31 January 2019
Published 20 March 2019
10.1126/sciadv.aav8423

Citation: Y. Cui, K. Zhou, D. Strugatsky, Y. Wen, G. Sachs, Z. H. Zhou, K. Munson, pH-dependent gating mechanism of the *Helicobacter pylori* urea channel revealed by cryo-EM. *Sci. Adv.* **5**, eaav8423 (2019).